


Article

# Estimation of Source Range and Location Using Ship-Radiated Noise Measured by Two Vertical Line Arrays with a Feed-Forward Neural Network

Moon Ju Jo <sup>1</sup>, Jee Woong Choi <sup>1,2,3</sup> and Dong-Gyun Han <sup>4,\*</sup> 

<sup>1</sup> Department of Marine Science and Convergence Engineering, Hanyang University ERICA, Ansan 15588, Republic of Korea; jmjnz@hanyang.ac.kr (M.J.J.); choijw@hanyang.ac.kr (J.W.C.)

<sup>2</sup> Department of Military Information Engineering, Hanyang University ERICA, Ansan 15588, Republic of Korea

<sup>3</sup> Department of Intelligence and Information Engineering, Hanyang University ERICA, Ansan 15588, Republic of Korea

<sup>4</sup> Research Center for Ocean Security Engineering and Technology, Hanyang University ERICA, Ansan 15588, Republic of Korea

\* Correspondence: dghandg@hanyang.ac.kr

**Abstract:** Machine learning-based source range estimation is a promising method for enhancing the performance of tracking both the dynamic and static positions of targets in the underwater acoustic environment using extensive training data. This study constructed a machine learning model for source range estimation using ship-radiated noise recorded by two vertical line arrays (VLAs) during the Shallow-water Acoustic Variability Experiment (SAVEX-15), employing the Sample Covariance Matrix (SCM) and the Generalized Cross Correlation (GCC) as input features. A feed-forward neural network (FNN) was used to train the model on the acoustic characteristics of the source at various distances, and the range estimation results indicated that the SCM outperformed the GCC with lower error rates. Additionally, array tilt correction using the array invariant-based method improved range estimation accuracy. The impact of the training data composition corresponding to the bottom depth variation between the source and receivers on range estimation performance was also discussed. Furthermore, the estimated ranges from the two VLA locations were applied to localization using trilateration. Our results confirm that the SCM is the more appropriate feature for the FNN-based source range estimation model compared with the GCC and imply that ocean environment variability should be considered in developing a general-purpose machine learning model for underwater acoustics.

**Keywords:** machine learning; feed-forward neural network; source range estimation; sample covariance matrix; generalized cross correlation; array tilt; bottom depth; ocean environment variability; source localization



**Citation:** Jo, M.J.; Choi, J.W.; Han, D.-G. Estimation of Source Range and Location Using Ship-Radiated Noise Measured by Two Vertical Line Arrays with a Feed-Forward Neural Network. *J. Mar. Sci. Eng.* **2024**, *12*, 1665. <https://doi.org/10.3390/jmse12091665>

Academic Editor: Sergei Chernyi

Received: 28 June 2024

Revised: 19 August 2024

Accepted: 15 September 2024

Published: 18 September 2024



**Copyright:** © 2024 by the authors. Licensee MDPI, Basel, Switzerland. This article is an open access article distributed under the terms and conditions of the Creative Commons Attribution (CC BY) license (<https://creativecommons.org/licenses/by/4.0/>).

## 1. Introduction

Various underwater source localization methods use a vertical line array (VLA), such as matched field processing (MFP), array invariant, and machine learning-based approaches. MFP, which can also be applied with a single receiver, estimates a source location by comparing a measured acoustic field with repeated simulations using varying input variables [1–5]. Bartlett MFP, a fundamental form of MFP, and Minimum Variance MFP, which reduces the ambiguity of side lobes, have been used to find the source location from the receiving array [1,2]. Multiple Constraints MFP [3,4] and Frequency-Difference MFP [5] have been proposed to mitigate the impact of mismatches between simulated and real environments. Array invariant utilizes the invariant property of beam-time migration data obtained from beamforming in shallow waveguides to estimate the source range [6–8]. This method does

not require prior knowledge of the environment, operates independently of acoustic propagation modeling, and demands low computational resources. Kim et al. (2021) [7] applied acoustic intensity, which is a three-axis vector quantity, to the array invariant method for source localization. However, the array invariant method assumes the waveguide invariant as 1, which can cause range estimation errors due to variations in the bottom slope and spatio-temporal variations in sound speed profile [9]. Byun et al. (2020) [10] proposed an adaptive array invariant considering the propagation angle dependency of the waveguide invariant. The machine learning-based method learns labeled source location information from massive measured or simulated data, and then it can estimate the source range when new data without location information are input [11–13]. In recent years, machine learning has been applied for acoustic source localization in the underwater environment [14–32]. Some studies have demonstrated that machine learning-based methods perform better than Bartlett MFP [14–16,18–20].

Many input features of the machine learning model have been used, such as the Sample Covariance Matrix (SCM) [14–21], Generalized Cross Correlation (GCC) [22], cepstrogram [22–24], frequency-domain pressure [25,26], pressure magnitude [27,28], time-frequency spectrogram [29,30] and time-domain waveform [31,32]. Except for the SCM and the GCC, the features are source-dependent, meaning that models trained by these features cannot be applied to another source not used in training data. On the other hand, the SCM and the GCC are source-independent in a linear time-invariant system by eliminating the magnitude and phase of the source. The model trained by the SCM has been proven to localize unknown sources in the underwater environment [14].

Underwater sound propagation varies with environmental conditions and their variabilities. Therefore, datasets based on measurements or simulations under various conditions are necessary. However, collecting sufficient datasets that reflect environmental variability such as bottom depth and the sound speed profile is challenging in field measurements. Therefore, there are efforts to supplement data through simulations [30,32] and approaches to decrease dependency on large datasets [21,26]. Moreover, array tilt induced by ocean currents leads to unexpected arrival time differences among receivers, which directly causes errors in labeling training data and range estimation performance [18]. Liu et al. (2020) [18] evaluated the environmental sensitivity of a multi-task learning convolutional neural network (CNN) using simulation data. They found that the array tilt of VLA was the most sensitive factor, followed by the bottom depth. Chen et al. (2021) [19] investigated the sensitivity of a CNN model to the sound speed profile and bottom depth and demonstrated that these factors degrade the range estimation performance.

In this paper, we applied ship-radiated noise, in the form of continuous waves transmitted through varying acoustic channels received by two VLAs, to train a machine learning-based range estimation model using two source-independent features. We investigated the effects of environmental variability and the tilt of the receiver array on underwater sound propagation and, consequently, on the accuracy of source range and location estimation. The results demonstrate the differences in range estimation performance due to the physical characteristics of the two input features and how the performance of a single model can be improved by correcting for systematic and environmental factors. This approach is crucial for enhancing the robustness of machine learning models in underwater acoustics, and it contributes to the selection, design, optimization, and interpretation of models for underwater target detection, identification, and localization. Section 2 introduces the experimental data, input features, the structure of the machine learning model and learning parameters, and the method of array tilt correction. The source range estimation and localization results are presented in Section 3, and Section 4 discusses the factors affecting the performance. Finally, the conclusion is given in Section 5.

## 2. Methods

### 2.1. Acoustic Data Collection

As the experimental data, we used the ship radiated noise from the research vessel Onnuri (R/V Onnuri), which was considered as a target to estimate the range. This noise was received by two VLAs moored apart during the Shallow-water Acoustic Variability Experiment (SAVEX-15), which was conducted in the shallow water environment with a bottom depth of approximately 100 m in the northeastern China Sea, approximately 100 km southwest of Jeju Island, Republic of Korea, from 14 to 28 May 2015. The experiment aimed to acquire acoustic data and environmental data for research on underwater communication, acoustics, and oceanography. To acquire the acoustic data, two VLAs, consisting of 16 elements with 3.75 m spacing (from 24 to 80 m depth), were deployed approximately 5.5 km apart. The experimental area consists of a sandy bottom with the following geoacoustic properties: density  $\rho_b = 1.97 \text{ g/cm}^3$ , sound speed  $c_b = 1800 \text{ m/s}$ , and attenuation coefficient  $\alpha_b = 0.94 \text{ dB}/\lambda$  [33]. The bathymetry was measured using a Multibeam Echosounder (MBES), as shown in Figure 1a.

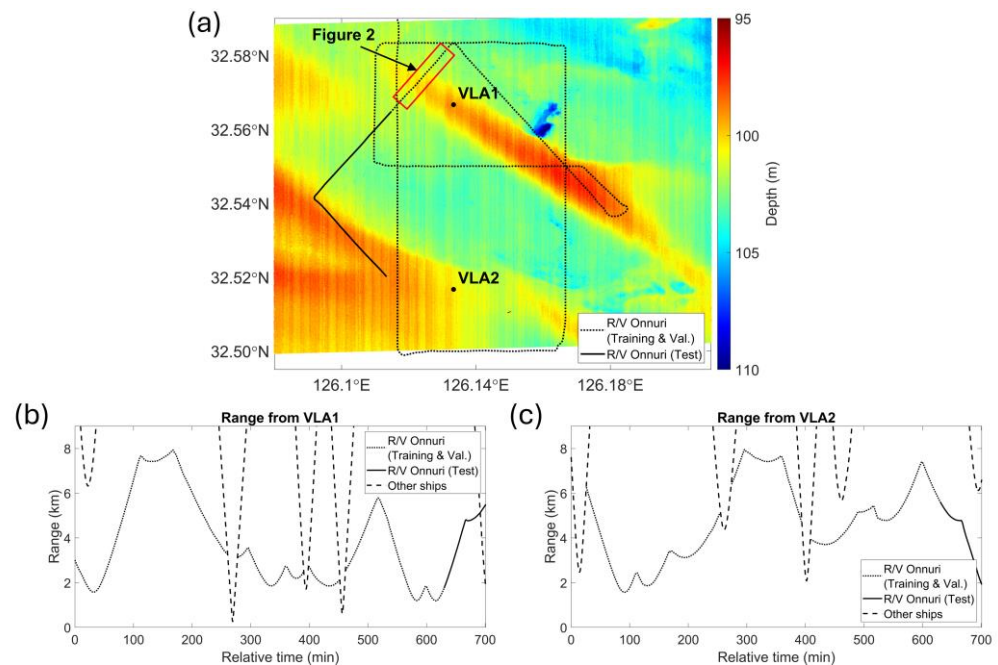


**Figure 1.** (a) Bathymetry of the experimental area and ship track of the R/V Onnuri. Range variations in the R/V Onnuri (b) from VLA1 and (c) from VLA2 as a function of time. The black dotted line represents the ship track and range variations used for the training and validation data, the black solid line corresponds to the test data, and the black dashed lines in the range variations represent other ships. The red box represents the ship track corresponding to the acoustic data analyzed in Figure 2.

During the experiment, although active sonar pings were sporadically transmitted from towed or moored projectors, we selected the period when the ship’s radiated noise was not affected by these transmitted signals. The ship track surrounding the two VLAs, which reflects relatively large variations in bottom depth between the source and receivers, was chosen (Figure 1a). For model training and validation, we used the data received by two VLAs from 11:33 to 22:03 UTC on 25 May 2015, spanning 630 min. The data corresponding to the periods when other ships were closer than the R/V Onnuri, based on the Automatic Identification System (AIS) data and Global Positioning System (GPS) data, were excluded (Figure 1b,c). For the validation, 10% of the training and validation data was randomly selected. The data from 22:03 to 23:13, spanning 70 min, was used for the test.

Figure 2 shows the acoustic characteristics of ship-radiated noise measured from VLA1 at a hydrophone depth of 25 m, which is the closest to the sea surface, as represented in the

spectrogram and spectrum level. These data are part of the training and validation sets and include sections where the R/V Onnuri approaches and then moves away. Generally, ship-radiated noise exhibits narrow band tonal components around 1 kHz and shows an increase in broadband energy due to amplitude modulation signals caused by the cavitation [34]. Particularly, when the ship approaches the receiver, passes the closest point of approach (CPA), and then moves away, this noise makes the symmetrical striation pattern in a spectrogram because of the interference with boundary reflected paths [35]. This pattern was clearly observed in our data. The median spectrum level, which represents the spectrum that lasted during the measurement period, was estimated from the spectral probability density with intensity average spectrum level in Figure 2b [36]. The narrow band tonal components of 985, 1322, and 1455 Hz were observed in the spectrum level, but the source of this feature was not evident. We selected the frequency range from 200 Hz to 1000 Hz to characterize the R/V Onnuri.

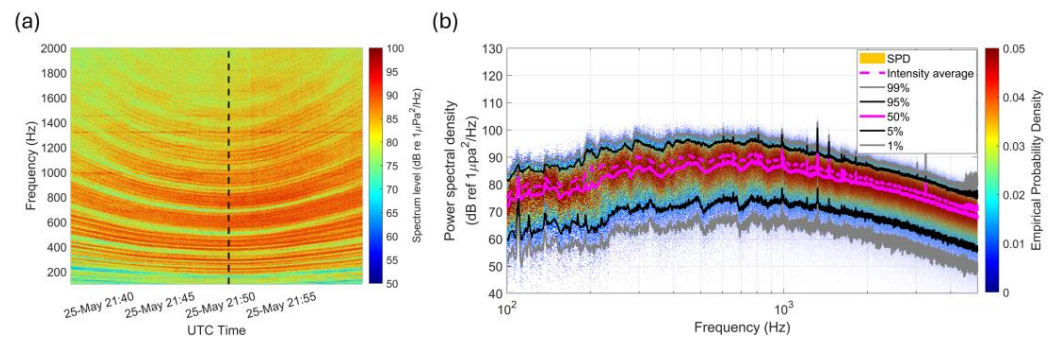


**Figure 2.** (a) Spectrogram of acoustic data measured from VLA1 at a depth of 25 m from May 25 21:35 to 21:59 UTC. The black thick dashed line represents the time of the closest point of approach (21:48 UTC). (b) The spectral probability density of acoustic data for 24 min. Thick magenta lines represents the average values of the mean intensity level (dashed) and the median spectrum level corresponding to the 50th percentile (solid).

### 2.2. Feature Extraction

In range-independent shallow water environments where the influence of environmental variability can be ignored, the underwater acoustic channel can be assumed to be a linear time-invariant system [1,37]. This implies ideal conditions without noise and temporal variations caused by sea surface fluctuations, varying sound speed profiles, or the movements of the source and receiver. The Fourier transform of the received signal at the  $j$ th element of the VLA and frequency  $f$  is given by [14]

$$R_j(f) = G(\vec{r}_j, \vec{r}_s, f)S(f) = G(\vec{r}_j, \vec{r}_s, f)|S(f)|e^{i\theta_s(f)} \tag{1}$$

where  $S(f)$  is the source spectrum,  $\theta_s(f)$  is the source phase in frequency domain, and  $G(\vec{r}_j, \vec{r}_s, f)$  is Green’s function corresponding to the source position  $\vec{r}_s$  and the  $j$ th receiver position  $\vec{r}_j$ .

To calculate the SCM, the  $R_j(f)$  are normalized by the Euclidean norm to eliminate the source magnitude [14].

$$\tilde{R}_j(f) = \frac{R_j(f)}{\sqrt{\sum_{n=1}^N |R_n(f)|^2}} = \frac{G(\vec{r}_j, \vec{r}_s, f)}{\sqrt{\sum_{n=1}^N |G(\vec{r}_n, \vec{r}_s, f)|^2}} e^{i\theta_s(f)} \tag{2}$$

The correlation between the  $\tilde{R}_j(f)$  and the  $\tilde{R}_k(f)$ —the normalized Fourier transform of the received signal at the  $k$ th receiver of the VLA—is calculated to eliminate the source

phase [14]. The asterisk in Equation (3) denotes the conjugate transpose operator. As a result, the SCM preserves the magnitude and phase term of Green’s function.

$$C_{j,k}^{SCM}(f) = \tilde{R}_j(f)\tilde{R}_k^*(f) = \frac{G(\vec{r}_j, \vec{r}_s, f)G^*(\vec{r}_k, \vec{r}_s, f)}{\sum_{n=1}^N |G(\vec{r}_n, \vec{r}_s, f)|^2} \quad (3)$$

To calculate the GCC, the correlation between the  $R_j(f)$  and the  $R_k(f)$  is multiplied by the weighting function  $W(f)$ , called the phase transform, which eliminates the source magnitude and phase [38]. As a result, the GCC preserves the phase term of Green’s function.

$$C_{j,k}^{GCC}(f) = W(f)R_j(f)R_k^*(f) = \frac{R_j(f)R_k^*(f)}{|R_j(f)R_k^*(f)|} = \frac{G(\vec{r}_j, \vec{r}_s, f)G^*(\vec{r}_k, \vec{r}_s, f)}{|G(\vec{r}_j, \vec{r}_s, f)G^*(\vec{r}_k, \vec{r}_s, f)|} \quad (4)$$

The SCM and the GCC were calculated using the acoustic data with a 1 s rectangular window every 10 s from the 16 elements of the two VLAs in a frequency range from 200 Hz to 1000 Hz with a 10 Hz interval, which is the dominant frequency band of the ship-radiated noise. The diagonal and upper triangular part of the  $16 \times 16$  SCM and the  $16 \times 16$  GCC were taken, divided into their real and imaginary parts, and concatenated into a one-dimensional vector for the model input. The concatenated size of each SCM and the GCC is 22,032, which is the product of 136 (the size of the diagonal and upper triangular matrix), 81 (the number of frequency components), and 2 (the real and imaginary parts).

### 2.3. Feed-Forward Neural Network

There is a nonlinear relationship between the input feature and the source range because of the varying underwater acoustic channel with environmental variability and multipath effects. A feed-forward neural network (FNN), a fundamental model widely used in machine learning applications, was used to model this nonlinear relationship. This model is a traditional neural network based on the universal approximation theorem, which demonstrates that a sufficiently deep and nonlinear neural network can approximate any continuous function on a compact domain with arbitrary precision [39]. The machine learning-based range estimation problem was treated as a classification problem in this study [14,15,17,19]. The range of the R/V Onnuri from the two VLAs was classified into 801 classes at 10 m intervals from 1 to 9 km. The input layer, corresponding to the size of the input feature, had 22,032 units [14]. Each of the two hidden layers had 5000 units, and the Exponential Linear Unit (ELU) was used for the activation function. The output layer had 801 units with softmax to represent the probability of each range class.

The network was trained for 100 epochs with a mini-batch size of 100. The learning rate was set to  $10^{-5}$ . As a learning strategy, early stopping was employed to prevent overfitting with patience value of 5. Categorical cross-entropy was used as the loss function [40], optimized with the Adam optimizer [41]. The training process was accelerated using a NVIDIA RTX A6000. The network was implemented using Tensorflow.

### 2.4. Correction for the Array Tilt Effect

The array tilt of VLA was influenced by tidal currents during SAVEX-15 [42]. Therefore, we conducted the simulations using a numerical acoustic propagation model with the sound speed profile and bathymetry measured in SAVEX-15 to evaluate the impact of array tilt on the range estimation errors with all other variables fixed (Appendix A). The Mean Absolute Percentage Error (MAPE), which is a widely used metric that measures the accuracy of a model by calculating the average absolute percentage difference between estimated and true values, was used to evaluate the range estimation error. The MAPE is defined as

$$MAPE \equiv \frac{100}{N} \sum_{i=1}^N \left| \frac{X_i - \hat{X}_i}{X_i} \right| \quad (5)$$



where  $X_i$  is the true target range based on GPS data,  $\hat{X}_i$  is the estimated target range, and  $N$  is the number of the samples. When the input feature was the SCM, the MAPE increased by over 10% as the absolute value of the array tilt angle exceeded  $\pm 3^\circ$ , and when the input feature was the GCC, the MAPE increased by over 50% as the angle exceeded  $\pm 2^\circ$ .

In this paper, the array tilt angle of two VLAs was estimated every minute using the array invariant method [8]. The array invariant method characterizes sound propagation in the multipath-dominant shallow water waveguide, and the array invariant parameter  $\chi$  is defined as [6]

$$\chi \equiv \frac{d}{dt}(\cos(\theta)) \tag{6}$$

where  $\theta$  is the beam angle and  $t$  is the arrival time of each path.  $\chi$  can be numerically estimated by fitting to the beam-time migration data (separated by the beam angle and the arrival time) with the least-squares approach. We applied an arbitrary tilt angle  $\theta_c$  to Equation (6) to compensate for the array tilt (Equation (7)).

$$\chi' \equiv \frac{d}{dt}(\cos(\theta - \theta_c)) \tag{7}$$

By varying  $\theta_c$  to find the fitting value that minimizes the error with the beam-time migration data, the estimated  $\theta_c$  was used to correct the arrival time by applying a time delay  $d\sin(\theta_c)/c$  for each receiver. Here,  $d$  denotes the distance from the anchor to the receiver and  $c$  represents the sound speed in water. We assumed that the source was far from the VLA and the array tilted in the direction of the source. From the array tilt angle estimated every minute, the outliers that occurred because of fitting failure were removed using a median filter with a window size of 10 (Figure 3). Consequently, the same time difference correction was applied to the six feature vectors extracted within each 1 min interval.

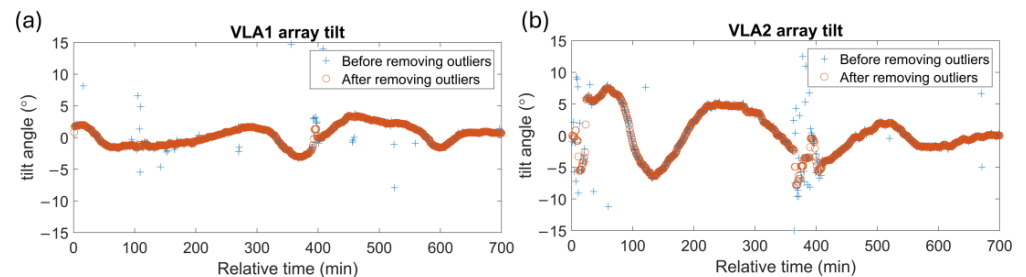


**Figure 3.** The estimated array tilt angle of the two VLAs, calculated every minute before (blue crosses) and after (orange circles) removing the outliers using a median filter with a window size of 10. (a) VLA1 and (b) VLA2.

### 3. Results

The source ranges were estimated using the FNN model with the SCM and the GCC as input features and compared to the ranges based on the GPS data. We expressed the range estimation results before and after correcting for the tilt effect and further categorized the performance into three groups based on the combination of VLA data used in the training data. First, the same VLA test was conducted, where the training and test data were from the same VLA (either VLA1 or VLA2) (Figure 4). Second, a different VLA test was conducted, where the training data were from one VLA (either VLA1 or VLA2) and the test was on the other (either VLA2 or VLA1) (Figure 5). Third, a large training data test was conducted, where the training data were from both VLAs, and the test was on either VLA1 or VLA2 (Figure 6). In addition, trilateration was used to localize source positions in two-dimensions (longitude and latitude) using the two estimated ranges for each case. The source position was determined at the intersection of two concentric circles centered at the two VLAs. This intersection resulted in two symmetric estimated positions, but only the position in the direction of the true bearing was used to analyze the error. If the circles did

not intersect, the source position could not be estimated. The errors in the range estimation and localization for the three tests, excluding instances of localization failure, are listed in Tables 1 and 2, respectively.

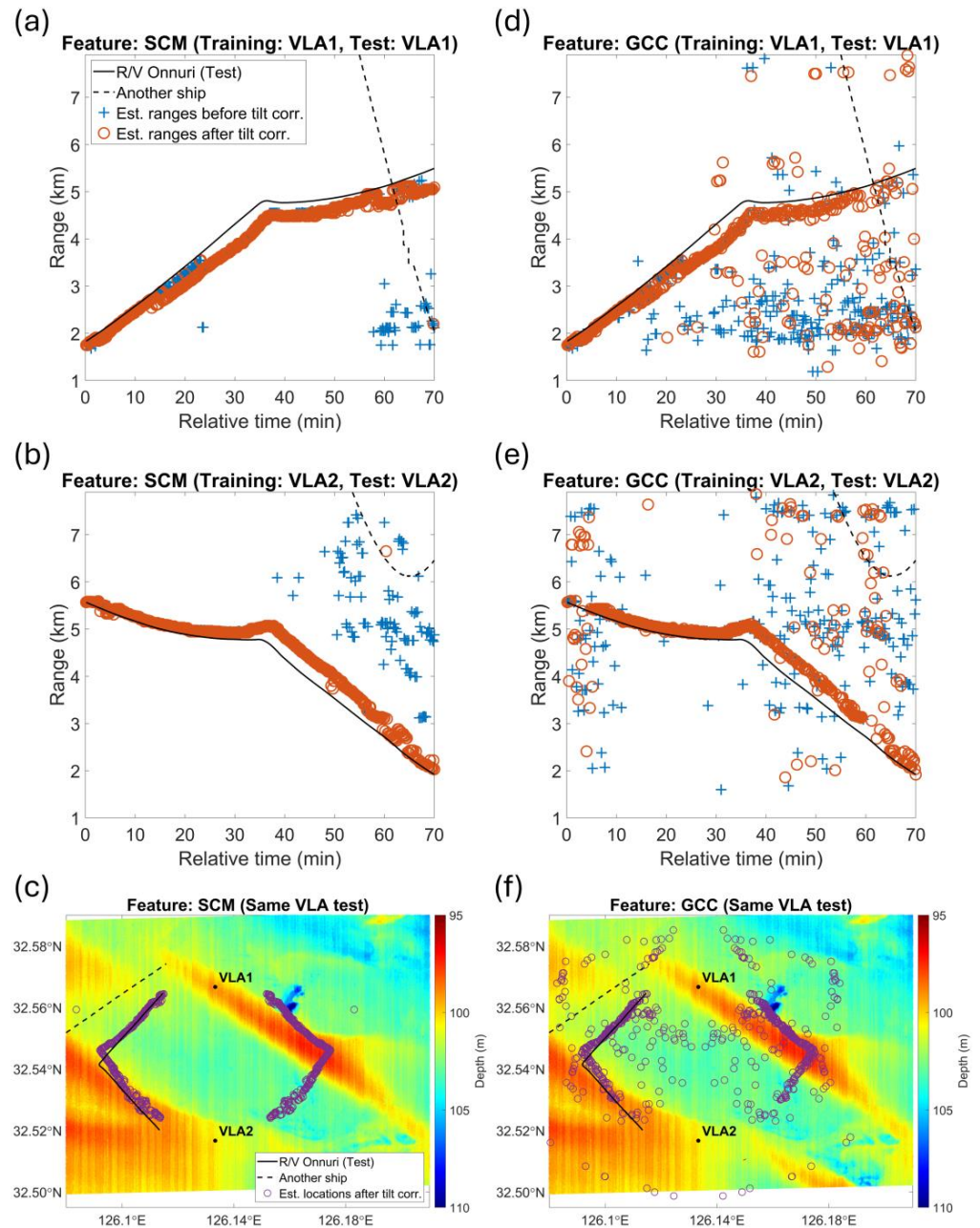


**Figure 4.** Source–receiver range estimation and localization results of the same VLA test. Range estimation results are shown for (a) the VLA1 test using the SCM, (b) the VLA2 test using the SCM, (d) the VLA1 test using the GCC, and (e) the VLA2 test using the GCC. Estimated ranges before and after tilt correction are represented by blue crosses and orange circles, respectively. Source localization results after tilt correction are represented by the purple circles in (c) when using the SCM and in (f) when using the GCC. The black solid line represents the ship track and range variations used for the test data. The black dashed line represents another ship during the test time.

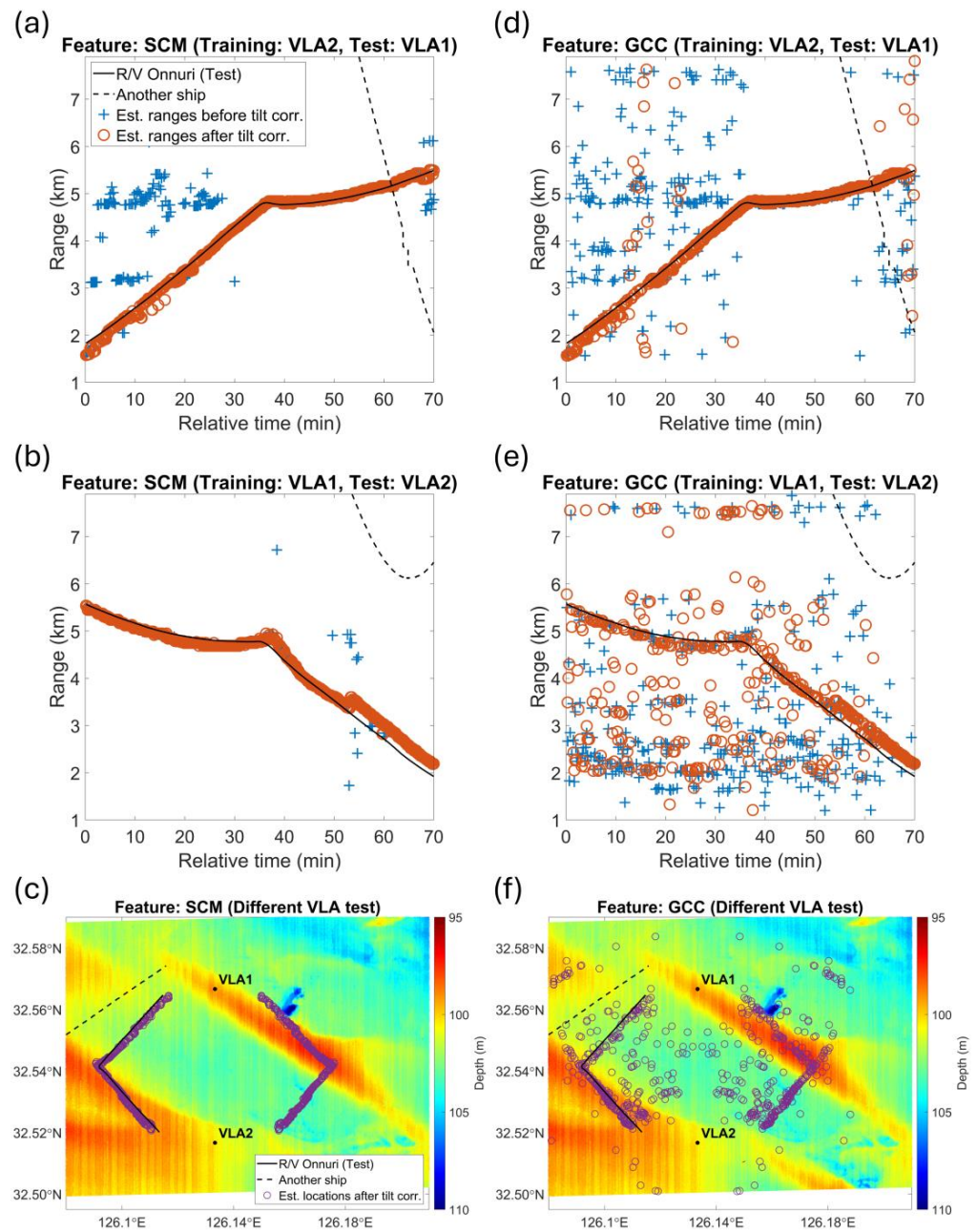


**Figure 5.** Source–receiver range estimation and localization results of the different VLA tests. Range estimation results are shown for (a) the VLA1 test using the SCM, (b) the VLA2 test using the SCM, (d) the VLA1 test using the GCC, and (e) the VLA2 test using the GCC. Estimated ranges before and after tilt correction are represented by blue crosses and orange circles, respectively. Source localization results after tilt correction are represented by the purple circles in (c) when using the SCM and in (f) when using the GCC. The black solid line represents the ship track and range variations used for the test data. The black dashed line represents another ship during the test time.



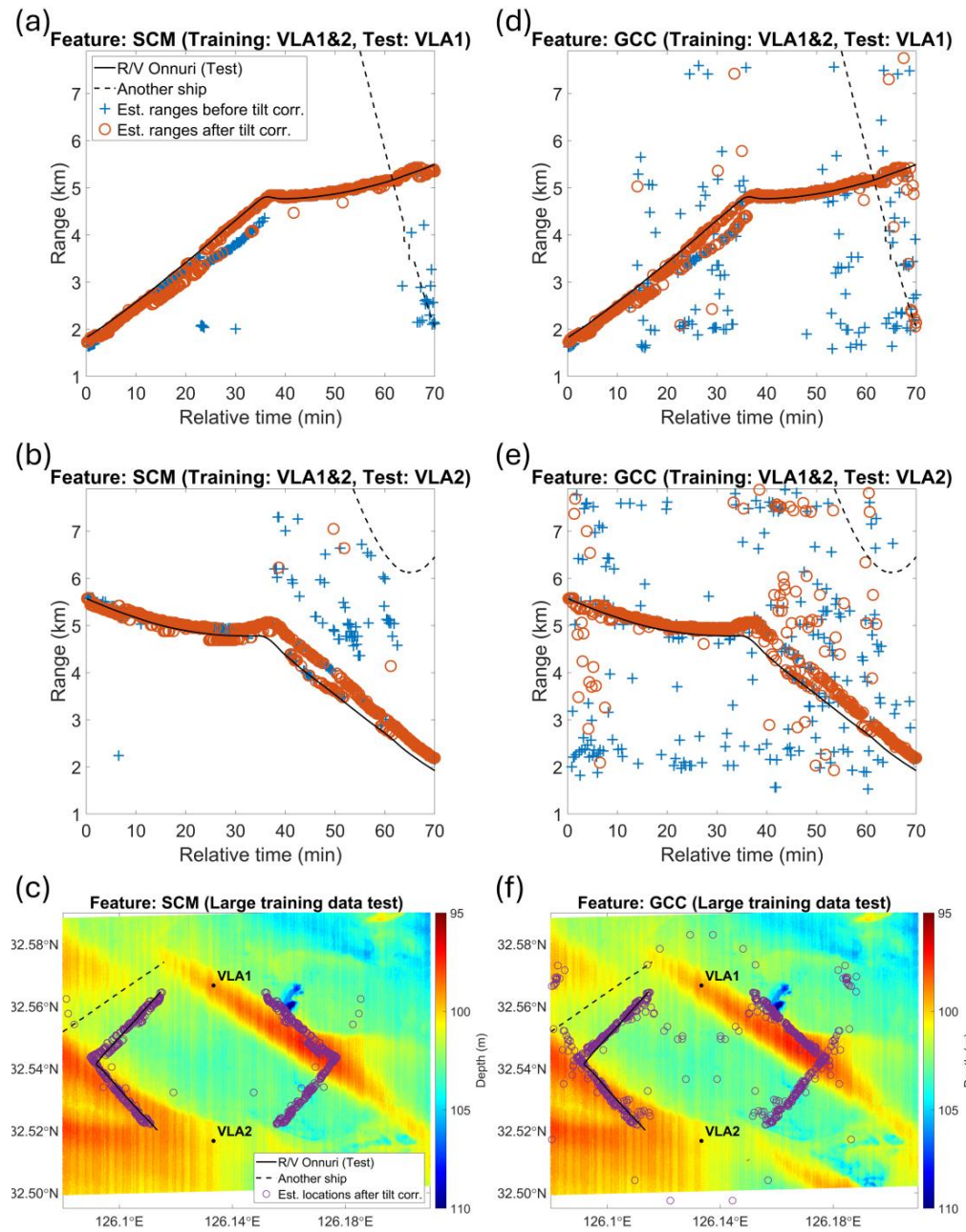


**Figure 6.** Source–receiver range estimation and localization results of the large training data test. Range estimation results are shown for (a) the VLA1 test using the SCM, (b) the VLA2 test using the SCM, (d) the VLA1 test using the GCC, and (e) the VLA2 test using the GCC. Estimated ranges before and after tilt correction are represented by blue crosses and orange circles, respectively. Source localization results after tilt correction are represented by the purple circles in (c) when using the SCM and in (f) when using the GCC. The black solid line represents the ship track and range variations used for the test data. The black dashed line represents another ship during the test time.

Machine learning using the SCM performed better and showed more consistent range estimation trends compared with using the GCC, with a minimum error reduction of 1.7% (the VLA1 test after array tilt correction with large data training) and a maximum error reduction of 31.3% (the VLA2 test before array tilt correction with VLA1 data training). Source localization performance using the SCM was also better than that using the GCC, with a minimum error reduction of 0.31 km (after array tilt correction in the large data training test) and a maximum error reduction of 1.36 km (before array tilt correction in the different VLA test). The superior performance of the SCM compared with the GCC

is attributed to the fact that the SCM includes both the magnitude and phase of Green’s function, providing more comprehensive information about channel impulse response (CIR) characteristics. In contrast, the GCC only incorporates phase information without the magnitude, resulting in relatively less information and limiting its ability to capture the characteristics of the CIR.

**Table 1.** MAPEs of estimated ranges before (in brackets) and after correction for the array tilt effect.

	Same VLA Test		Different VLA Test		Large Training Data Test	
	VLA1	VLA2	VLA2	VLA1	VLA1&2	
Training	VLA1	VLA2	VLA1	VLA2	VLA1	VLA2
SCM	7.2 (11.8)	6.7 (29.1)	2.2 (20.7)	4.2 (5.0)	3.3 (7.0)	6.3 (13.2)
GCC	17.0 (27.9)	19.6 (38.3)	6.1 (32.4)	22.4 (36.3)	5.0 (13.8)	13.4 (25.7)

**Table 2.** Mean localization errors (km) before (in brackets) and after correction for the array tilt effect.

	Same VLA Test		Different VLA Test		Large Training Data Test	
	VLA1	VLA2	VLA2	VLA1	VLA1&2	
SCM	0.42 (1.11)	0.42 (1.11)	0.16 (0.70)	0.16 (0.70)	0.28 (0.58)	0.28 (0.58)
GCC	1.12 (1.96)	1.12 (1.96)	0.95 (2.06)	0.95 (2.06)	0.59 (1.24)	0.59 (1.24)

Correcting for the array tilt effect contributed to performance improvement, especially when other ship locations were identified from approximately 60 to 70 min in both the VLA1 and VLA2 tests. In the case of the SCM, range estimation accuracy was improved by a minimum of 0.8% and a maximum of 22.4%, and localization accuracy was improved by 0.51 km on average because of array tilt correction.

For the same VLA test results in Figure 4, the range was underestimated for both the SCM and GCC when using VLA1 for the training and test data, but it was overestimated when using VLA2 for the training and test data. For the different VLA test results in Figure 5, the bias observed in the same VLA test was somewhat mitigated, especially for VLA1. Notably, using the SCM as the feature for training with VLA2 and testing on VLA1 yielded the best performance across all tests. Conversely, using the GCC as the feature for training with VLA1 and testing on VLA2 resulted in the worst performance. For the large training data test results in Figure 6, biased range errors were still conspicuous in the VLA 2 test. The bias between the true values and the estimations is presumed to be due to the limited training data composition, which is discussed in the next section. The range estimation accuracy from the different VLA tests was better than that from the same VLA test, indicating that the machine learning model is robust to the sensor’s position. The performance of the large training data test was better than the same VLA test but worse than the different VLA test, indicating that larger data did not guarantee performance improvement in this study. The reason why the performance was not the best despite using the largest amount of training data is also discussed in the next section.

#### 4. Discussion

We estimated the range from the two VLAs to the ship using a machine learning model with two features, and the localization results directly reflected the range estimations. The comparison of results from two features involved evaluating a model trained with both magnitude and phase information (SCM) against a model trained with phase information alone (GCC). While the SCM might be expected to perform better because of the additional information it includes, our results quantitatively confirmed this expectation through application to the experimental data. Furthermore, the results from the three tests (the same

VLA test, a different VLA test, and a large training data test) indicated that the performance of the VLA1 test in the different VLA test was better than the large training data test. This is because the training data used in the VLA1 test had average bottom depths more similar to those in the test data in the different VLA test (left in Figure 7b). Relative bottom depth refers to the difference between the average depth of the source-receiver range in the test data and that in the training data. Although the large training data test included more datasets at various ranges, the average depth at those ranges differed significantly from the test data, resulting in worse performance.

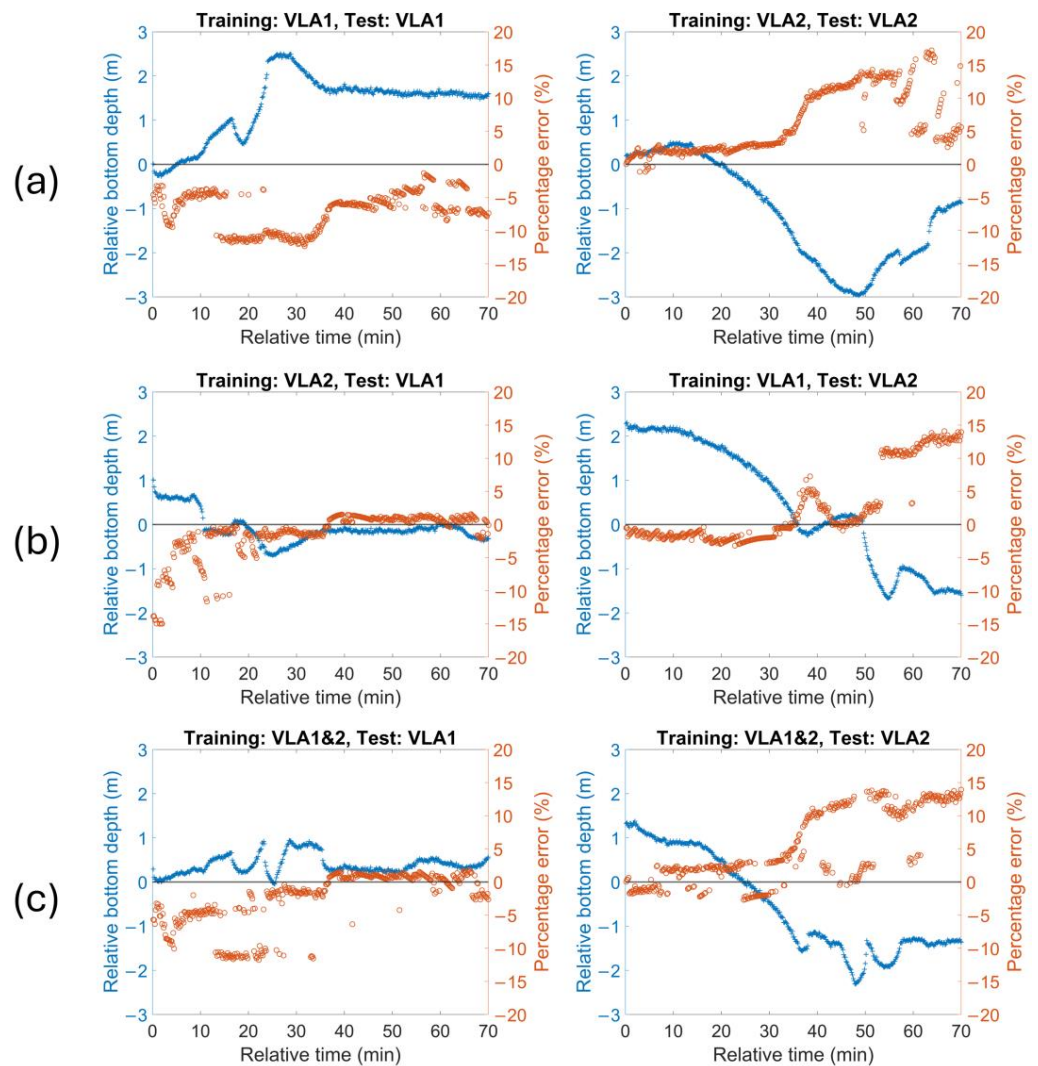


**Figure 7.** Variations in the relative bottom depth and the percentage error of the range estimation as a function of the time of the test data (feature: SCM after tilt correction). (a) The same VLA test, (b) the different VLA test, and (c) the large training data test. Relative bottom depth and percentage error are represented by blue crosses and orange circles, respectively.

Similar to the examination of the array tilt effects, the simulation conducted to identify the bottom depth effect (Appendix B) shows that there is a negative relationship between the percentage error of the estimated range and the relative bottom depth of the test data compared with the training data at the same source range. The biased errors observed in the experiment results (Figures 4–6) are also explained by this negative relationship because of the effect of the relative bottom depth (Figure 7). This indicates that the quality of the training data, reflecting ocean environmental variability, is more important than applying

a large quantity of data that does not account for this variability. The bias in the range estimation is even observed in the results using MFP [43].

As mentioned above, the bottom depth at the same source range causes biased range estimation from the ground truth range, so we applied data resampling to improve the range estimation performance. In the training data used for the large training data test, there was a greater amount of data with relatively deep bottom depths compared with data with relatively shallow bottom depths, as shown in the distribution of the average bottom depth and the source range (Figure 8a). Data resampling (over-sampling when the amount of data is under 10 and under-sampling when the amount of data is over 10) was applied to mitigate the error by the bottom depth difference with or without the tilt correction (Figure 8b). The MAPE exhibited a decreasing trend by the data resampling when the input feature was the SCM (Table 3), and we confirmed that resampling with 10 and 20 samples showed similar levels of improvement in the range estimations. It is necessary to obtain the training data (simulation or measurement) corresponding to missing source ranges and bottom depths to construct a model that exhibits better range estimation performance on the test data with previously unidentified source ranges and bottom depths.

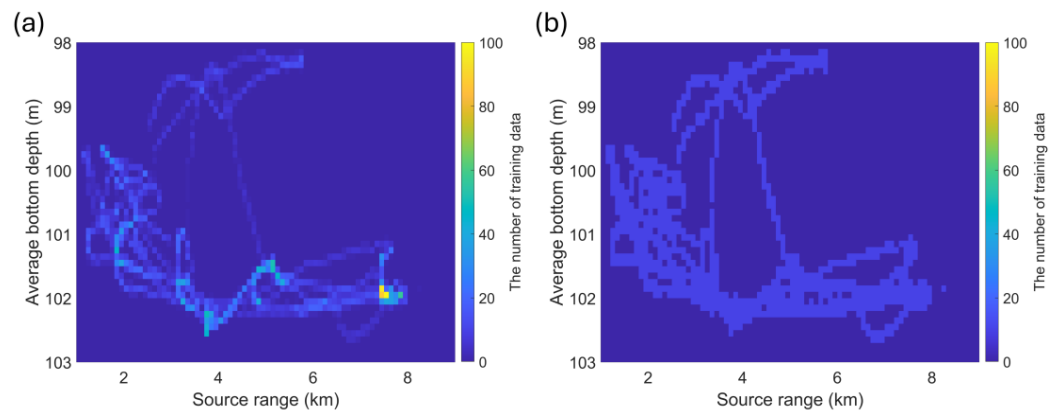


**Figure 8.** The training data distribution as a function of the average bottom depth and the source range obtained from VLA1 and VLA2: (a) before data resampling and (b) after data resampling.

**Table 3.** MAPEs of the estimated ranges before and after data resampling when the input feature is the SCM. Brackets denote before correction for the array tilt effect.

Training	VLA1&2		Resampling VLA1&2	
	VLA1	VLA2	VLA1	VLA2
Test				
SCM	3.3 (7.0)	6.3 (13.2)	3.7 (6.7)	4.9 (11.8)

The array tilt was estimated using the array invariant method, and range estimation and localization results were improved by correcting the arrival time difference. Although we considered the relative bottom depth effect, many environmental variables remain in underwater acoustic propagation. The sound speed profile exhibits spatio-temporal variability, and the bottom depth and the geoacoustic parameters exhibit spatial variability. Therefore, sufficient data collection to encompass environmental variations is necessary to construct an adaptive range estimation model, as the features labeled by range are derived from received signals transmitted through this environment. Yoon et al. [44] proposed OceanPINN, which predicts the acoustic pressure field in the ocean based on the measured data at a few sampled points, assuming a range-independent environment, utilizing Physics-Informed Neural Networks (PINNs) [45]. PINNs predict unknown data using a governing partial differential equation and limited training data, by discerning



the underlying dynamics of the data, with the potential to be applied in underwater acoustics [13].

As mentioned in Section 1, the two features used in this study are source-independent. However, since Green's function is frequency-dependent, our model is applicable within the limited frequency bandwidth we used. While it may be possible to achieve some level of performance in adjacent frequency bands, applications with significant frequency differences may result in failed range estimation. Additionally, it is necessary to investigate whether the model is applicable to narrowband signals within the used frequency band. These limitations suggest that although the features are defined as source-independent, the spectral characteristics of the training and test data can influence range estimation performance, indicating that they cannot be considered perfectly independent. Although the GCC performs worse than the SCM, the GCC could be used to estimate the direction of arrival. Ferguson et al. [24] proposed using cepstrum-based features combined with the GCC as the input feature for source localization, which performs better than the GCC only. Moreover, features extracted from a 1 s time window of acoustic data received by 16 channels can cause variations in estimation performance. Therefore, the impact of the time window length, the number of receivers, and their spacing needs to be studied.

We used an FNN as the machine learning model for range estimation and compared input features that have a source independency in the linear time-invariant system (SCM and GCC). Liu et al. (2021) [20] proposed a Gated Feedback Gated Recurrent Unit for measuring range and depth of the source, performing better than a FNN in the mismatched array tilt environment. Ge et al. (2022) [21] proposed label distribution-guided transfer learning, which uses a limited amount of the measured data for training, supplemented by pre-training the network with simulation data from a known environment. We applied the Support Vector Machine (SVM) classifier with a hinge loss function, regularization parameter  $C = 1$ , and a One-vs.-Rest scheme [46] for multiclass classification for range estimation after tilt correction (Appendix C). The range estimation results using SVM had relatively higher MAPEs compared with those using the FNN, and the trend that the SCM is better than the GCC remained consistent. However, these results derived from the data, features, and models should not be generalized to all cases. Moreover, it is possible that the performance could be improved by optimizing the hyperparameters through algorithms such as random search and grid search [47]. Other models, including widely used models (CNN, Residual Network, and Recurrent Neural Network) and learning strategies can be studied for adaptation to the varying underwater environment.

In this study, basic trilateration was conducted using the estimated ranges from two points, which inherently has the limitation of ambiguity due to symmetrical positions. To improve this, additional range estimations from at least one more point are necessary. These localization results can be applied to advanced techniques such as extended Kalman filters and particle filters to improve target tracking performance [48–50].

## 5. Conclusions

We utilized a machine learning-based method to estimate the source range and location using ship-radiated noise from two VLAs and compared the results of two source-independent features including the SCM and the GCC. Our results showed that the SCM, which includes both magnitude and phase information, outperformed the GCC, which only incorporates phase information, with a maximum error reduction of 31.3% and 1.36 km in the estimation of the source range and location, respectively. The error of the source range and location estimation was reduced by up to 26.3% and 1.11 km, respectively, by correcting for the array tilt effect. Despite these advancements, differences in average bottom depth were identified as a factor causing bias between the measured and estimated values, and the impact of average bottom depth discrepancies between the training and test data on range estimation accuracy was verified by simulations. This study has meaningful implications resulting from its direct comparison of SCM and GCC within a machine learning framework for source range estimation in underwater acoustics. To mitigate

the remaining biases and errors, future research should investigate additional models and features that enhance robustness against environmental variability. Augmenting and reconstructing training data to account for temporal and spatial variability is essential. Furthermore, recent advancements in underwater target detection and identification have employed multi-modal deep learning techniques using two or more features, which could also be applied to the estimation of source range and localization [51]. Our findings can be instrumental in selecting appropriate features for such applications, demonstrating the importance of considering both magnitude and phase information for improved performance. Additionally, the proposed method can be combined with Target Motion Analysis (TMA) research to enhance underwater target tracking and management.

**Author Contributions:** Conceptualization, M.J.J., J.W.C. and D.-G.H.; data curation, M.J.J.; formal analysis, M.J.J.; funding acquisition, J.W.C.; investigation, M.J.J. and D.-G.H.; methodology, M.J.J.; project administration, J.W.C.; supervision, J.W.C. and D.-G.H.; validation, J.W.C. and D.-G.H.; visualization, M.J.J.; writing—original draft, M.J.J., J.W.C. and D.-G.H.; writing—review and editing, D.-G.H. All authors have read and agreed to the published version of the manuscript.

**Funding:** This work was supported by a Korea Research Institute for defense Technology planning and advancement (KRIT) grant funded by the Defense Acquisition Program Administration (DAPA) in 2024 (No. KRIT-CT-22-056, Study on the signal modeling and reproduction of the marine life sound) and a National Research Foundation of Korea (NRF) grant funded by the Korea government (MSIT) (2020R1A2C2007772).

**Institutional Review Board Statement:** Not applicable.

**Informed Consent Statement:** Not applicable.

**Data Availability Statement:** The original contributions presented in this study are included in this article. Further inquiries can be directed to the corresponding author.

**Acknowledgments:** The authors thank T. L. Song, S. Shin, and Y. G. Yoon for their comments on this research and D. H. Lee, H. Sul, and W. Shin for their assistance with data analysis.

**Conflicts of Interest:** The authors declare no conflicts of interest.

## Abbreviations

Following abbreviations are used in this study.

VLA	vertical line array
SAVEX-15	Shallow-water Acoustic Variability Experiment
SCM	Sample Covariance Matrix
GCC	Generalized Cross Correlation
MFP	matched field processing
CNN	convolutional neural network
MBES	Multibeam Echosounder
AIS	Automatic Identification System
GPS	Global Positioning System
CPA	closest point of approach
FNN	feed-forward neural network
ELU	Exponential Linear Unit
MAPE	Mean Absolute Percentage Error
CIR	channel impulse response
PINN	Physics-Informed Neural Network
SVM	Support Vector Machine
TMA	Target Motion Analysis
CTD	Conductivity–Temperature–Depth

## Appendix A

We fixed the array tilt angle of the VLA as observed from the source in the training data as  $0^\circ$  and varied the angle in the test data from  $-5^\circ$  to  $5^\circ$  to observe the impact of the

array tilt on the range estimation in the SAVEX-15 experimental environment. The other variables referred to the SAVEX-15 experimental environment (Table A1). The source was assumed to be a pure tone of 600 Hz, which is the median frequency of the R/V Onnuri noise distribution band, and the source depth was set to 5 m to simulate the noise of a ship at the sea surface [8]. For array tilt simulation, assuming the acoustic ray parallel to the sea surface, a signal received by a sensor at a distance  $d$  from the seabed with an array tilt angle  $\theta$  and a sound speed  $c$  incurred a time delay of  $d\sin(\theta)/c$ . The sound speed  $c$  was set to 1505 m/s, the average of the sound speed profile. We trained and tested the machine learning model with the SCM and the GCC derived by ray-based acoustic transmission modeling (BELLHOP). In total, 10% of the training and validation data were used as the validation data. For the numerical evaluation, the MAPE of the estimated range according to the array tilt change was solved (Figure A1).

**Table A1.** Simulation parameters for array tilt effect test.

	Training and Validation Data	Test Data
Source	600 Hz sinusoidal wave	
Source depth (m)	5	
Receiver depth (m)	23.5:3.75:79.75	
Array tilt (°)	0	−5:1:5
Source range (km)	1:0.01:7	
Geoacoustic parameter	$\rho_b = 1.97 \text{ g/cm}^3, c_b = 1800 \text{ m/s}, \alpha_b = 0.94 \text{ dB}/\lambda$	
Bottom depth (m)	100	
Sound speed profile	Measured by Conductivity–Temperature–Depth (CTD) cast at the SAVEX-15 experimental site on 25 May 2015 at UTC 07:11	

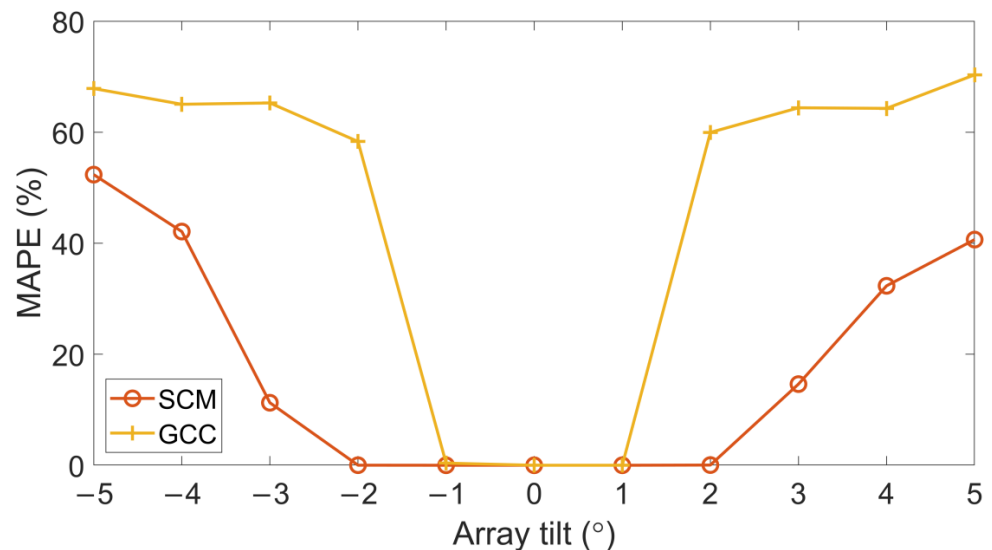


**Figure A1.** MAPEs of estimated ranges according to the array tilt change.

### Appendix B

We fixed the bottom depth from the source to the VLA in the training data as 100 m and varied the bottom depth in the test data from 97 m to 103 m to observe the impact of the bottom depth on the range estimation in the SAVEX-15 experimental environment. The other variables referred to the SAVEX-15 experimental environment (Table A2). The array tilt of the VLA was fixed at 0°. We trained and tested the machine learning model with the SCM and the GCC derived by BELLHOP. In total, 10% of the training and validation data were used as the validation data. Figure A2 shows the estimated range when the relative

bottom depths are  $-3$  m,  $-2$  m,  $-1$  m,  $1$  m,  $2$  m, and  $3$  m. For the numerical evaluation, the percentage errors of the estimated ranges as a function of the relative bottom depth were solved (Figure A3).

**Table A2.** Simulation parameters for the bottom depth effect test.

	Training and Validation Data	Test Data
Source	600 Hz sinusoidal wave	
Source depth (m)	5	
Receiver depth (m)	23.5:3.75:79.75	
Array tilt ( $^{\circ}$ )	0	
Source range (km)	1:0.01:7	
Geoacoustic parameter	$\rho_b = 1.97 \text{ g/cm}^3$ , $c_b = 1800 \text{ m/s}$ , $\alpha_b = 0.94 \text{ dB}/\lambda$	
Bottom depth (m)	100	97:1:103
Sound speed profile	Measured by Conductivity–Temperature–Depth (CTD) cast at the SAVEX-15 experimental site on 25 May 2015 at UTC 07:11	

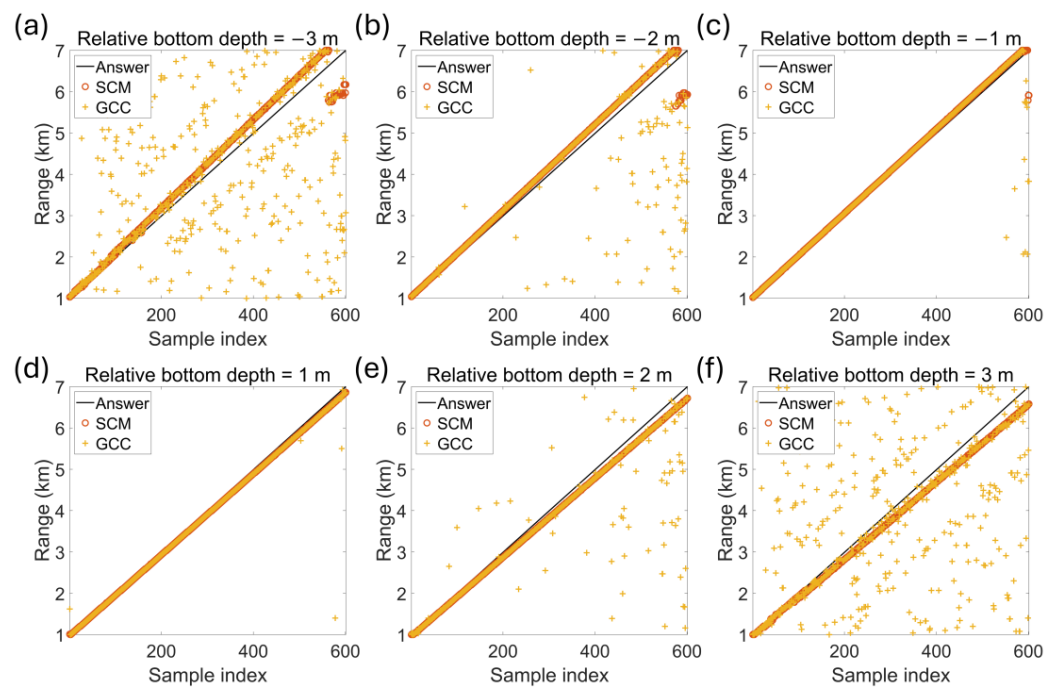


**Figure A2.** Estimated ranges when the relative bottom depths are (a)  $-3$  m, (b)  $-2$  m, (c)  $-1$  m, (d)  $1$  m, (e)  $2$  m, and (f)  $3$  m.



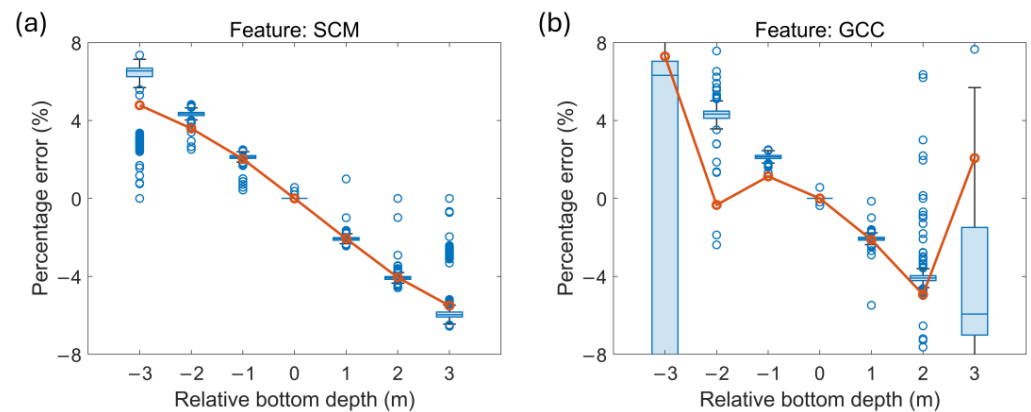


**Figure A3.** Box plot of percentage errors of the estimated ranges according to the relative bottom depth when the input feature is (a) the SCM or (b) the GCC. Within each box, horizontal lines denote median values; boxes extend from the 25th percentile to the 75th percentile of percentage errors; vertical extending lines denote adjacent values (i.e., the most extreme values within the 1.5 interquartile range of the 25th and 75th percentiles of percentage errors); dots denote observations outside the range of adjacent values. The orange line denotes the mean value.

### Appendix C

**Table A3.** MAPE comparison of estimated ranges after array tilt correction using FNN and SVM, respectively. Bold red denotes the best MAPE for each input features.

	Same VLA Test		Different VLA Test		Large Training Data Test	
	VLA1	VLA2	VLA2	VLA1	VLA1&2	
Training	VLA1	VLA2	VLA1	VLA2	VLA1	VLA2
SCM	<b>7.2</b> /13.0	<b>6.7</b> /9.0	<b>2.2</b> /3.4	<b>4.2</b> /10.3	<b>3.2</b> /6.5	<b>6.3</b> /11.1
GCC	17.0/ <b>13.0</b>	19.6/ <b>11.4</b>	6.1/ <b>4.0</b>	22.4/ <b>11.6</b>	<b>5.0</b> /6.6	13.4/ <b>10.7</b>

### References

- Jensen, F.B.; Kuperman, W.A.; Porter, M.B.; Schmidt, H. *Computational Ocean Acoustics*, 2nd ed.; Springer Science & Business Media: New York, NY, USA, 2011; pp. 733–749.
- Baggeroer, A.B.; Kuperman, W.A.; Mikhalevsky, P.N. An Overview of Matched Field Methods in Ocean Acoustics. *IEEE J. Ocean. Eng.* **1993**, *18*, 401–424. [\[CrossRef\]](#)
- Schmidt, H.; Baggeroer, A.B.; Kuperman, W.A.; Scheer, E.K. Environmentally Tolerant Beamforming for High-resolution Matched Field Processing: Deterministic Mismatch. *J. Acoust. Soc. Am.* **1990**, *88*, 1851–1862. [\[CrossRef\]](#)
- Byun, G.; Hunter Akins, F.; Gemba, K.L.; Song, H.C.; Kuperman, W.A. Multiple Constraint Matched Field Processing Tolerant to Array Tilt Mismatch. *J. Acoust. Soc. Am.* **2020**, *147*, 1231–1238. [\[CrossRef\]](#) [\[PubMed\]](#)
- Worthmann, B.M.; Song, H.C.; Dowling, D.R. High Frequency Source Localization in a Shallow Ocean Sound Channel Using Frequency Difference Matched Field Processing. *J. Acoust. Soc. Am.* **2015**, *138*, 3549–3562. [\[CrossRef\]](#)
- Lee, S.; Makris, N.C. The Array Invariant. *J. Acoust. Soc. Am.* **2006**, *119*, 336–351. [\[CrossRef\]](#)
- Kim, S.; Cho, S.; Jung, S.; Choi, J.W. Passive Source Localization Using Acoustic Intensity in Multipath-Dominant Shallow-Water Waveguide. *Sensors* **2021**, *21*, 2198. [\[CrossRef\]](#)
- Byun, G.; Kim, J.S.; Cho, C.; Song, H.C.; Byun, S.-H. Array Invariant-Based Ranging of a Source of Opportunity. *J. Acoust. Soc. Am.* **2017**, *142*, EL286–EL291. [\[CrossRef\]](#)
- Hahn, J.; Park, J.S.; Kim, J.S. Estimation Error of Target Range Using Array Invariant. In Proceedings of the Acoustical Society of Korea, Busan, Republic of Korea, 1–3 November 2023; p. 36.
- Byun, G.; Song, H.C. Adaptive Array Invariant. *J. Acoust. Soc. Am.* **2020**, *148*, 925–933. [\[CrossRef\]](#)
- Bianco, M.J.; Gerstoft, P.; Traer, J.; Ozanich, E.; Roch, M.A.; Gannot, S.; Deledalle, C.-A. Machine Learning in Acoustics: Theory and Applications. *J. Acoust. Soc. Am.* **2019**, *146*, 3590–3628. [\[CrossRef\]](#)
- Yang, H.; Lee, K.; Choo, Y.; Kim, K. Underwater Acoustic Research Trends with Machine Learning: Passive SONAR Applications. *J. Ocean Eng. Technol.* **2020**, *34*, 227–236. [\[CrossRef\]](#)
- Niu, H.; Li, X.; Zhang, Y.; Xu, J. Advances and Applications of Machine Learning in Underwater Acoustics. *Intell. Mar. Technol. Syst.* **2023**, *1*, 8. [\[CrossRef\]](#)

14. Niu, H.; Reeves, E.; Gerstoft, P. Source Localization in an Ocean Waveguide Using Supervised Machine Learning. *J. Acoust. Soc. Am.* **2017**, *142*, 1176–1188. [[CrossRef](#)] [[PubMed](#)]
15. Niu, H.; Ozanich, E.; Gerstoft, P. Ship Localization in Santa Barbara Channel Using Machine Learning Classifiers. *J. Acoust. Soc. Am.* **2017**, *142*, EL455–EL460. [[CrossRef](#)] [[PubMed](#)]
16. Wang, Y.; Peng, H. Underwater Acoustic Source Localization Using Generalized Regression Neural Network. *J. Acoust. Soc. Am.* **2018**, *143*, 2321–2331. [[CrossRef](#)] [[PubMed](#)]
17. Chi, J.; Li, X.; Wang, H.; Gao, D.; Gerstoft, P. Sound Source Ranging Using a Feed-Forward Neural Network Trained with Fitting-Based Early Stopping. *J. Acoust. Soc. Am.* **2019**, *146*, EL258–EL264. [[CrossRef](#)] [[PubMed](#)]
18. Liu, Y.; Niu, H.; Li, Z. A Multi-Task Learning Convolutional Neural Network for Source Localization in Deep Ocean. *J. Acoust. Soc. Am.* **2020**, *148*, 873–883. [[CrossRef](#)] [[PubMed](#)]
19. Chen, R.; Schmidt, H. Model-Based Convolutional Neural Network Approach to Underwater Source-Range Estimation. *J. Acoust. Soc. Am.* **2021**, *149*, 405–420. [[CrossRef](#)] [[PubMed](#)]
20. Liu, Y.; Niu, H.; Yang, S.; Li, Z. Multiple Source Localization Using Learning-Based Sparse Estimation in Deep Ocean. *J. Acoust. Soc. Am.* **2021**, *150*, 3773–3786. [[CrossRef](#)]
21. Ge, F.-X.; Bai, Y.; Li, M.; Zhu, G.; Yin, J. Label Distribution-Guided Transfer Learning for Underwater Source Localization. *J. Acoust. Soc. Am.* **2022**, *151*, 4140–4149. [[CrossRef](#)]
22. Ferguson, E.L.; Williams, S.B.; Jin, C.T. Sound Source Localization in a Multipath Environment Using Convolutional Neural Networks. In Proceedings of the IEEE International Conference on Acoustics, Speech and Signal Processing, Calgary, AB, Canada, 15–20 April 2018; pp. 2386–2390. [[CrossRef](#)]
23. Ferguson, E.L.; Williams, S.B.; Jin, C.T. Convolutional Neural Network for Single-Sensor Acoustic Localization of a Transiting Broadband Source in Very Shallow Water. *J. Acoust. Soc. Am.* **2019**, *146*, 4687–4698. [[CrossRef](#)]
24. Ferguson, E.L. Multitask Convolutional Neural Network for Acoustic Localization of a Transiting Broadband Source Using a Hydrophone Array. *J. Acoust. Soc. Am.* **2021**, *150*, 248–256. [[CrossRef](#)] [[PubMed](#)]
25. Lefort, R.; Real, G.; Drémeau, A. Direct Regressions for Underwater Acoustic Source Localization in Fluctuating Oceans. *Appl. Acoust.* **2017**, *116*, 303–310. [[CrossRef](#)]
26. Wang, W.; Ni, H.; Su, L.; Hu, T.; Ren, Q.; Gerstoft, P.; Ma, L. Deep Transfer Learning for Source Ranging: Deep-Sea Experiment Results. *J. Acoust. Soc. Am.* **2019**, *146*, EL317–EL322. [[CrossRef](#)] [[PubMed](#)]
27. Niu, H.; Gong, Z.; Ozanich, E.; Gerstoft, P.; Wang, H.; Li, Z. Deep-Learning Source Localization Using Multi-Frequency Magnitude-Only Data. *J. Acoust. Soc. Am.* **2019**, *146*, 211–222. [[CrossRef](#)] [[PubMed](#)]
28. Liu, W.; Yang, Y.; Xu, M.; Lü, L.; Liu, Z.; Shi, Y. Source Localization in the Deep Ocean Using a Convolutional Neural Network. *J. Acoust. Soc. Am.* **2020**, *147*, EL314–EL319. [[CrossRef](#)]
29. Thode, A.M.; Kim, K.H.; Blackwell, S.B.; Greene, C.R.; Nations, C.S.; McDonald, T.L.; Macrander, A.M. Automated Detection and Localization of Bowhead Whale Sounds in the Presence of Seismic Airgun Surveys. *J. Acoust. Soc. Am.* **2012**, *131*, 3726–3747. [[CrossRef](#)]
30. Neilsen, T.B.; Escobar-Amado, C.D.; Acree, M.C.; Hodgkiss, W.S.; Van Komen, D.F.; Knobles, D.P.; Badiy, M.; Castro-Correa, J. Learning Location and Seabed Type from a Moving Mid-Frequency Source. *J. Acoust. Soc. Am.* **2021**, *149*, 692–705. [[CrossRef](#)] [[PubMed](#)]
31. Van Komen, D.F.; Neilsen, T.B.; Howarth, K.; Knobles, D.P.; Dahl, P.H. Seabed and Range Estimation of Impulsive Time Series Using a Convolutional Neural Network. *J. Acoust. Soc. Am.* **2020**, *147*, EL403–EL408. [[CrossRef](#)] [[PubMed](#)]
32. Goldwater, M.; Zitterbart, D.P.; Wright, D.; Bonnel, J. Machine-Learning-Based Simultaneous Detection and Ranging of Impulsive Baleen Whale Vocalizations Using a Single Hydrophone. *J. Acoust. Soc. Am.* **2023**, *153*, 1094–1107. [[CrossRef](#)] [[PubMed](#)]
33. Song, H.C.; Cho, C. Array Invariant-Based Source Localization in Shallow Water Using a Sparse Vertical Array. *J. Acoust. Soc. Am.* **2017**, *141*, 183–188. [[CrossRef](#)]
34. Urlick, R.J. *Principles of Underwater Sound*, 3rd ed.; MacGraw-Hill: New York, NY, USA, 1983.
35. Brekhovskikh, L.M.; Lysanov, Y.P. *Fundamentals of Ocean Acoustics*; Springer: New York, NY, USA, 2003. [[CrossRef](#)]
36. Merchant, N.D.; Barton, T.R.; Thompson, P.M.; Pirodda, E.; Dakin, D.T.; Dorocijz, J. Spectral probability density as a tool for ambient noise analysis. *J. Acoust. Soc. Am.* **2013**, *133*, EL262–EL267. [[CrossRef](#)] [[PubMed](#)]
37. Bonnel, J.; Thode, A.; Wright, D.; Chapman, R. Nonlinear time-warping made simple: A step-by-step tutorial on underwater acoustic modal separation with a single hydrophone. *J. Acoust. Soc. Am.* **2020**, *147*, 1897–1926. [[CrossRef](#)] [[PubMed](#)]
38. Knapp, C.; Carter, G. The Generalized Correlation Method for Estimation of Time Delay. *IEEE Trans. Acoust. Speech Signal Process.* **1976**, *24*, 320–327. [[CrossRef](#)]
39. Kidger, P.; Lyons, T. Universal Approximation with Deep Narrow Networks. In Proceedings of the Thirty Third Conference on Learning Theory, Graz, Austria, 9–12 July 2020; pp. 2306–2327.
40. Ho, Y.; Wookey, S. The real-world-weight cross-entropy loss function: Modeling the costs of mislabeling. *IEEE Access* **2019**, *8*, 4806–4813. [[CrossRef](#)]
41. Kingma, D.P.; Ba, J. Adam: A method for stochastic optimization. *arXiv* **2014**, arXiv:1412.6980.
42. Park, J.; Seong, W.; Yang, H.; Nam, S.; Lee, S.-W. Array Tilt Effect Induced by Tidal Currents in the Northeastern East China Sea. *Ocean. Eng.* **2019**, *194*, 106654. [[CrossRef](#)]

43. D'spain, G.L.; Murray, J.J.; Hodgkiss, W.S.; Booth, N.O.; Schey, P.W. Mirages in Shallow Water Matched Field Processing. *J. Acoust. Soc. Am.* **1999**, *105*, 3245–3265. [[CrossRef](#)]
44. Yoon, S.; Park, Y.; Gerstoft, P.; Seong, W. Predicting Ocean Pressure Field with a Physics-Informed Neural Network. *J. Acoust. Soc. Am.* **2024**, *155*, 2037–2049. [[CrossRef](#)]
45. Raissi, M.; Perdikaris, P.; Karniadakis, G.E. Physics-Informed Neural Networks: A Deep Learning Framework for Solving Forward and Inverse Problems Involving Nonlinear Partial Differential Equations. *J. Comput. Phys.* **2019**, *378*, 686–707. [[CrossRef](#)]
46. Bishop, C.M. *Pattern Recognition and Machine Learning*; Springer: Berlin, Germany, 2006.
47. Bergstra, J.; Bengio, Y. Random Search for Hyper-Parameter Optimization. *J. Mach. Learn. Res.* **2012**, *13*, 281.
48. Julier, S.J.; Uhlmann, J.K. Unscented Filtering and Nonlinear Estimation. *Proc. IEEE* **2004**, *92*, 401–422. [[CrossRef](#)]
49. Del Moral, P. Nonlinear Filtering: Interacting Particle Resolution. *Comptes Rendus l'Académie Sci.-Ser. I-Math.* **1997**, *325*, 653–658. [[CrossRef](#)]
50. Sul, H.; Jo, M.J.; Song, T.L.; Choi, J.W. Array Invariant-Based Range-Only Target Motion Analysis for Ship Noise Measured by Two Vertical Line Arrays in Shallow Water. *J. Acoust. Soc. Am.* **2023**, *153*, A300. [[CrossRef](#)]
51. Ngiam, J.; Khosla, A.; Kim, M.; Nam, J.; Lee, H.; Ng, A.Y. Multimodal deep learning. In Proceedings of the 28th International Conference on Machine Learning (ICML-11), Bellevue, Washington, DC, USA, 28 June–2 July 2011; pp. 689–696.

**Disclaimer/Publisher's Note:** The statements, opinions and data contained in all publications are solely those of the individual author(s) and contributor(s) and not of MDPI and/or the editor(s). MDPI and/or the editor(s) disclaim responsibility for any injury to people or property resulting from any ideas, methods, instructions or products referred to in the content.